

Transpiration Cooling Heat Transfer Experiments in Laminar and Turbulent Hypersonic Flows

Imran Naved ^{*}, Tobias Hermann[†], Chris Hambidge[‡], Hassan Saad Ifti[§], Chiara Falsetti[¶], and Matthew McGilvray^{||}
University of Oxford, Oxford, England OX2 0ES, United Kingdom

Iullia S Tirichenko^{**}, and Luc Vandeperre^{††}
Imperial College London, Department of Materials & Centre for Advanced Structural Ceramics, London, SW7 2AZ, UK

The design of a transpiration cooled system requires detailed local heat transfer information on and in the vicinity of the porous injector; however, limited spatially resolved experimental studies exist, particularly in hypersonic flows. In this work experiments were conducted in the Oxford High Density Tunnel at Mach 6.1 in both laminar and turbulent regimes. Spatially resolved 2D surface heat transfer measurements were acquired by imaging directly on and downstream of two micro-porous transpiration cooled injectors (METAPOR CE170 and Zirconia) using high-speed infra-thermography. Whilst injection in the laminar regime results in a steady, monotonic reduction in heat transfer from the start of the injector, a flatter profile is present for the turbulent cases where turbulent mixing inhibits surface heat transfer reduction. It was found that a modification to existing relations from film theory successfully correlates the stream-wise heat transfer distribution on the injector for different blowing rates of Nitrogen and Helium injection. A key result is that Helium performs much better than reported in previous experiments. Finally, the downstream thermal effectiveness is characterised for turbulent flows. A collapse of the thermal effectiveness is achieved and a modified analytical correlation proposed.

Nomenclature

B_h	Blowing parameter
c_p	Specific heat capacity, $\text{J kg}^{-1} \text{K}^{-1}$
C^*	Chapman-Rubens factor at the Eckert reference temperature; $(T_e/T^*)(\mu^*/\mu_e)$
F	Blowing ratio, $(\rho_c u_c)/(\rho_e u_e)$

^{*}D.Phil. Student, Oxford Thermofluids Institute, University of Oxford, AIAA member

[†]Departmental Lecturer, Oxford Thermofluids Institute, University of Oxford, AIAA member

[‡]Research Assistant, Oxford Thermofluids Institute, University of Oxford, AIAA member

[§]DPhil student, Oxford Thermofluids Institute, University of Oxford, AIAA member

[¶]Post-doctoral Research Assistant, Oxford Thermofluids Institute, University of Oxford, AIAA member

^{||}Associate Professor, Oxford Thermofluids Institute, University of Oxford, AIAA member

^{**}Post-doctoral Research Assistant, Imperial College London

^{††}Professor of Structural Ceramics, Imperial College London

k	Thermal conductivity, $\text{W m}^{-1} \text{K}^{-1}$
K_D	Darcy coefficient, m^2
K_F	Forchheimer coefficient, m
L	Thickness, m
M	Mach number
M	Molecular weight, g mol^{-1}
\dot{q}	Heat flux, W m^{-2}
Re	Reynolds number
s	Stream-wise length of injector, m
SEM	Scanning electron microscope
St	Stanton number
T	Temperature, K
TPS	Thermal protection system
u	Velocity, m s^{-1}
UHTC	Ultra High Temperature Ceramic
x	Distance from the leading edge, m
x'	Streamwise distance from the start of the injector, m
x_s	Start of the porous injector, m
y	Lateral distance from the model centreline, m
θ	Ratio of coefficients with and without mass transfer, defined by Eq (1)
ϕ	A dimensionless mass transfer rate, defined by Eq (1)
ε	Emissivity
ϕ	Porosity
ρ	Density, kg m^{-3}
η	Effectiveness, defined by Eq (13)
μ	Viscosity, $\text{Pa} \cdot \text{s}$
ξ	Correlation parameter, defined by Eq (14)
$\bar{\chi}$	Viscous interaction parameter; $\frac{M^3}{\sqrt{Re}} \sqrt{\frac{\rho_w \mu_w}{\rho_e \mu_e}}$
<i>Subscript</i>	
0	Uncooled reference
e	Gas at boundary layer edge
f	Coolant fluid

I. Introduction

During ascent, cruise and reentry, aerospace vehicles travelling at hypersonic speeds are subject to extremely high heat fluxes due to aerodynamic heating [1]. A large fraction of the mass budget is devoted to the thermal protection system (TPS) to protect the vehicle from failure. Although heat sinks (passive) and ablation (semi-passive) are successful for vehicles operated at present, conventional thermal protection systems often have a low degree of reusability, especially on nose tips and leading edges where the vehicle experiences high peak heating. For certain vehicles, such as atmospheric cruise and glide vehicles, maintaining aerodynamic performance and reusability is highly important. In particular, many of these vehicles utilise radar or optical sensors and require a viewing port or window of some optically or radar transparent material. Ablation products from ablative insulators tend to obscure the sensor's view which means that such TPS systems cannot be used ahead of or in the vicinity of such windows [2].

For these scenarios, a potential active TPS system is transpiration cooling. This involves passing a fluid through a porous material onto the external boundary layer. The cooling process is achieved through four primary effects: heat from the wall is convected out by the fluid, the coolant creates a thin film which thickens the boundary layer and insulates the wall from the hot external gas, the coolant film can protect the wall from surface oxidation, and allowing for higher wall temperatures enables re-radiation and reduces surface catalytic heating. However, a transpiration cooled system requires a considerable quantity of gas under high pressure, a manifold, and a cooling control system. There are large cost, weight, reliability, and volume penalties associated with these systems which must be carefully balanced against potential benefits.

There is a vast amount of work in the literature regarding this topic spanning more than 70 years. Transpiration cooling has been successfully applied to nose cones and frustums of hypersonic vehicles [3, 4] as well as for the walls of scramjet combustors [5]. However, relatively little work has considered the two-dimensional spatial effects of a transpiration cooled injector beginning downstream of the leading edge. Such a scenario would occur if transpiration cooling is applied to the internal wall of a scramjet combustor or placed in the vicinity of an optical window. Furthermore, there is a substantial geometric difference between injectors with holes of the order $100\mu\text{m}$ [6] and modern micro-porous materials with pore diameters of $< 10\mu\text{m}$ [7]. A uniform film coverage over and downstream of the injector is essential to ensure the target region is kept below critical temperature limits.

To enable designers to assess the viability of a transpiration cooled system for such situations, there is a need to build up a detailed two-dimensional experimental data-set in hypersonic conditions. Previously, two-dimensional data has been achieved by placing a large number of discrete heat transfer gauges in between the holes on a transpiration cooled wall [6, 8]. However, for modern micro-porous materials, discrete gauges are likely to disturb the coolant outflow

distribution and a non-intrusive measurement technique is highly desirable. In more recent years, low speed infrared thermography has been employed in long duration, supersonic facilities [5, 9] but, additionally, testing in short duration hypersonic tunnels is desirable.

In this work, the spatial two-dimensional surface heat transfer of a transpiring porous injector was measured experimentally on a flat plate at Mach 6.1 in laminar and turbulent conditions. Two porous injectors made of METAPOR CE170 and Zirconia were tested. The surface heat transfer on and downstream of the porous injector was measured using high-speed infrared thermography employing the same technique described in Naved et al. [10]. For the first time, a modification to existing relations from film theory is proposed that accounts for the growth of the boundary layer at the start of the injector. The surface heat transfer on the injector is successfully correlated across different blowing rates for Nitrogen and Helium injection. In addition, for the turbulent boundary layer, the thermal film effectiveness downstream of the injector is measured and subsequently correlated across different blowing rates.

II. Theoretical Approach

Over the course of transpiration cooling research in the past 70 years, various models have been proposed to predict the surface heat transfer reduction on transpiring porous media in both subsonic and hypersonic flows at laminar and turbulent conditions. Perhaps the simplest of those models is film theory developed by Mickley [11] in which the ratio of transport coefficients (whether that is heat, mass, or momentum) is predicted by making an idealisation that the transition between the main-stream and the wall occur entirely within a thin laminar film of thickness, Δ , lying immediately adjacent to the wall. The thickness of this film is not predicted by film theory but rather is defined as the thickness which would offer the experimentally observed resistance to the transfer processes. Thus, the variation in transfer coefficients may be written in the form

$$\theta = \frac{\phi}{e^{\phi} - 1} \quad (1)$$

where θ is the ratio of the coefficient with and without mass transfer and ϕ is a dimensionless mass transfer rate. For heat transfer, the function in Eq. (1) is written in the form

$$\frac{St}{St_0} = \frac{B_h}{e^{B_h} - 1} \quad (2)$$

where B_h is a blowing parameter defined as

$$B_h = \frac{F}{St_0}. \quad (3)$$

St_0 is the Stanton number in the absence of injection (i.e. when $F = 0$) and F is the blowing ratio which is the ratio

of the coolant mass flux to the free stream mass flux at the boundary layer edge

$$F = \frac{\rho_f u_f}{\rho_e u_e} \quad (4)$$

where ρ and u are density and velocity respectively. The subscripts (f) and (e) refer to the injected gas and the boundary layer edge conditions respectively. Film theory makes no assumption about the state of the boundary layer and the results of film theory have been applied in the past for both laminar and turbulent regimes [11, 12] with a reasonable agreement to experimental data. Moyer and Rindal [13] noted that a slight modification of the above equation as follows

$$St = St_0 \cdot \left[\frac{0.8B_h}{e^{0.8B_h} - 1} \right] \quad (5)$$

yielded a better fit to experimental data for turbulent flows.

Whilst film theory gives reasonable predictions with injection of an identical gas to the freestream, injection of a foreign gas requires a correction. The most common correction is either a correction for the ratio of molecular weights between the injected and freestream gas, (M_e/M_f), or the ratio of specific heat capacities, ($c_{p,f}/c_{p,e}$). The logic behind a correction factor is that a lower molecular mass would result in a larger blockage effect, as there is a greater volume of lighter gas in the boundary layer for the same mass flow rate whilst the higher the specific heat capacity, the greater the quantity of heat absorbed for the same mass-flow rate. Without knowledge of the surface concentration of coolant, nor the relative weights of these two variables to the overall change in heat transfer, the effect of foreign gas injection may be accounted for purely as a molecular weight factor (M_e/M_f). This approach has been successfully employed in previous studies though there is some variation in how the correction factor is weighted to achieve a good fit with experimental data [6, 14].

The other drawback of film theory is that it is assumed that injection begins at the leading edge and continues downstream for the full extent of the flat plate. However, in many cases, the injector is likely to be of a finite length, beginning at a point downstream of the leading edge. An approach suggested by Stalmach et al. [3] for laminar flows is that the blowing parameter defined above may be modified by a factor $((x - x_s)/x)^{0.5}$ where x is the distance from the leading edge and x_s is the location of the start of the injector. This hearkens to a similar approach in laminar and turbulent downstream film effectiveness theory [15–17]. In the same way, it is proposed that for turbulent flows, the factor may be expressed as $((x - x_s)/x)^{0.8}$. Thus, the film theory relation above may be rewritten for a finite length injector for laminar flows

$$St = St_0 \cdot \left[\frac{\lambda}{e^\lambda - 1} \right], \quad \lambda = C \cdot B_h \cdot \left[\frac{x - x_s}{x} \right]^{0.5} \cdot \left[\frac{M_e}{M_f} \right]^m \quad (6)$$

and for turbulent flows

$$St = St_0 \cdot \left[\frac{\omega}{e^\omega - 1} \right], \quad \omega = D \cdot B_h \cdot \left[\frac{x - x_s}{x} \right]^{0.8} \cdot \left[\frac{M_e}{M_f} \right]^n. \quad (7)$$

The factors C , D , m and n are constants which need to be determined either experimentally or numerically for a given freestream flow condition. The application of this modified relation to experimental data is explored further in Section IV.C.

III. Experimental Methodology

A. Experimental Model

Experimental testing was conducted on a flat plate model used in previous studies [18–21] at 0° angle of attack. Figure 1 shows a schematic of the experimental model. A porous injector of $39.5 \times 39.5 \text{ mm}^2$ was placed 160 mm downstream of the model sharp leading edge (see Section III.B for more details about the injector). A plenum is located underneath the injector and pipework placed to feed the injection gas to the injector. The temperature and pressure in the plenum was measured by a fast response (response time $< 0.1 \text{ ms}$) K-type thermocouple ($\varnothing 0.762 \text{ mm}$) and a Kulite pressure transducer (HEL-375-35BARA). Downstream of the porous injector, the model features a 340 mm long PEEK surface for downstream infrared measurements (material properties in Table 1). For a secondary verification of the surface heat transfer, 13 quartz based platinum individual thin film gauges are mounted both upstream and downstream of the porous injector as well as one OMEGA CO2-K surface mounted thermocouple. The thermocouple is made from 0.13 mm thermocouple alloy and has a response time in the range of 2-5 ms. Finally, 3D printed trips may be added to a pocket 25.7 mm downstream of the leading edge to aid transition for the turbulent test cases. A diamond transition trip was used with a span-wise length of 90 mm and a height of 0.1 mm. A flush insert was used for the laminar experiments.

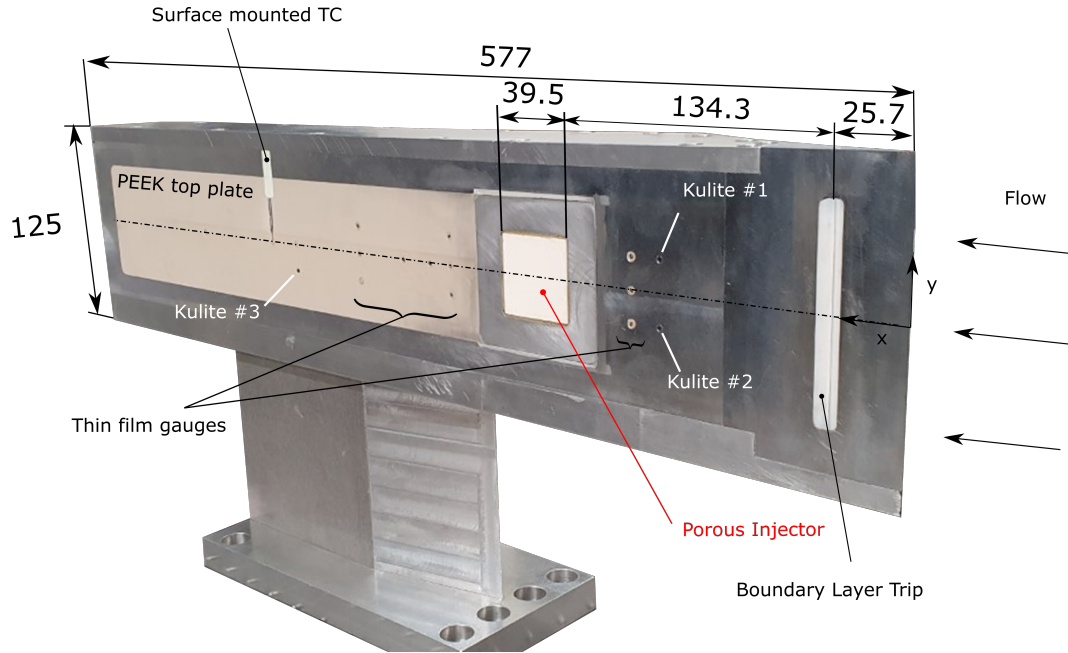


Fig. 1 Flat plate model instrumented with Kulite pressure transducers, thin film gauges and a porous injector with a PEEK top plate for infrared measurements. Dimensions in mm.

In addition, the surface static pressure was measured using two surface mounted Kulite pressure transducers (XCS-093-5A). The Total temperature was measured in the test section using differentially heated aspirated thermocouples. The measured data was acquired using a National Instruments PXIe-8135 controller with one PXIe-6368 card. A sample rate of 125 kHz was used to record all signals of the measurement which includes model and wind tunnel instrumentation. A separate heat transfer amplifier unit, HTA5, is also used for thin film gauge data acquisition. This forms a stand alone unit, run at a matching sample rate to the main DAQ system.

Primarily, surface heat transfer measurements were acquired using infrared thermography and a schematic of the optical setup is shown in Fig. 2. The experimental test piece is orientated in vertical configuration such that the field of view (FoV) of the IR camera is nearly normal to the model surface. Two infrared cameras are used for these experiments, the FLIR A6751 SLS long-wave infrared (LWIR) camera with a wavelength band of $7.5\text{--}11\mu\text{m}$ fitted with a 17 mm lens and a Telops M3K FAST mid-wave infrared (MWIR) camera with a wavelength range of $1.5\text{--}5.2\mu\text{m}$ fitted with a 100 mm lens. The LWIR camera was used to give a broad image of the flat plate including up to 100 mm downstream of the porous injector whereas the MWIR camera was used to complement the LWIR camera with detailed close up images of the porous sample. Due to the spectral emissivity dependence of porous Zirconia (the emissivity of Zirconia is very low in the mid-wave region), it was only possible to obtain LWIR images for the tests with the Zirconia injector. The experimental model was viewed through a 50 mm coated germanium and 100 mm sapphire window respectively for the long-wave and mid-wave cameras. The LWIR camera was operated at a windowed spatial resolution of 256×320 at a frame rate of 400 Hz and the MWIR operated at 320×254 with a frame rate of 2 kHz. This corresponds to

approximately 7 pixels/mm with the MWIR and 2 pixels/mm with the LWIR camera.

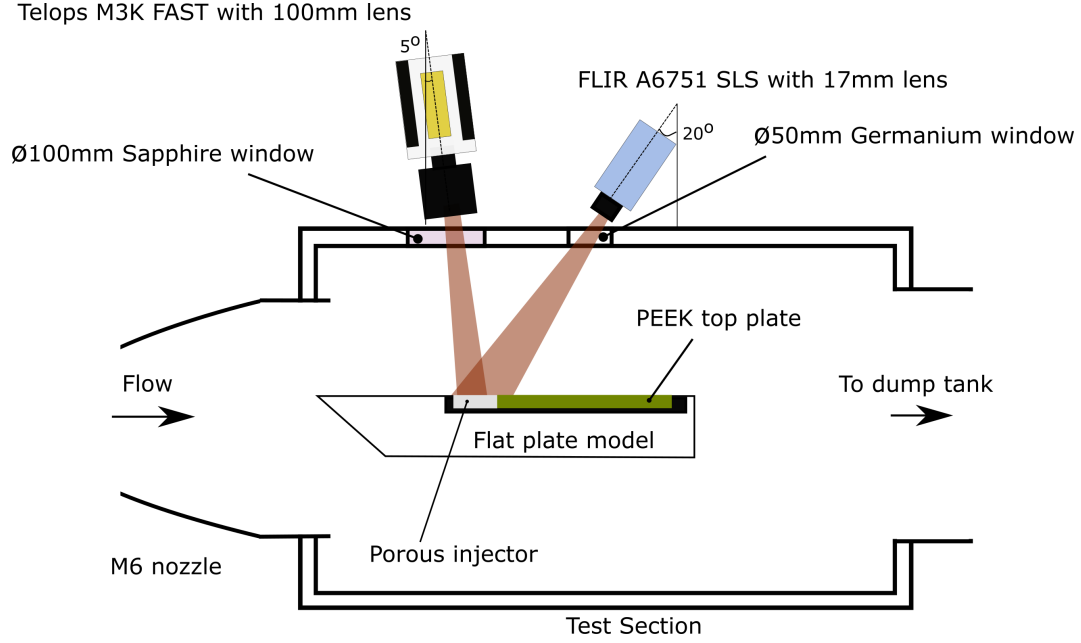


Fig. 2 Top view of the experimental model in the test section.

B. Porous Injector

Various porous materials have been used for transpiration cooling experiments including Ultra-High-Temperature-Ceramic (UHTCs) such as ZrB_2 [7] and carbon-carbon (C/C) composites [22]. ZrBr_2 in particular is a candidate flight material with a melting point of 3505 K and the extremely fine pore structure (on the order of $1\mu\text{m}$) which allows for a very even injection with no localized jets from fissures in the material. However, the high thermal product of this material leads to very low signal to noise ratio for infrared measurements in transient hypersonic wind tunnels. Thus, an alternative material for the purpose of wind tunnel experiments with a similar internal structure (pore diameters of the order of $2\mu\text{m}$) but higher conductivity is porous Zirconia (ZrO_2) manufactured by Imperial College London. Yttria-Stabilized Zirconia, $3\text{--}5\mu\text{m}$ was sintered in air at 1200°C for 45 minutes yielding a 40% porous substrate. The resulting sample combines a very low thermal product with the pore size and therefore outflow homogeneity of candidate materials for transpiration cooling. An alternative, commercially available micro-porous material is METAPOR CE170 which is made of aluminium hydroxide bonded to a resin system (pore diameter $20\mu\text{m}$). This material has an order of magnitude larger pore sizes than Zirconia (Fig. 3) and is an interesting material for comparison as the cooling effectiveness of porous injectors may be a function of surface geometry, roughness and coolant outflow. The properties of both materials are summarised in Table 1.

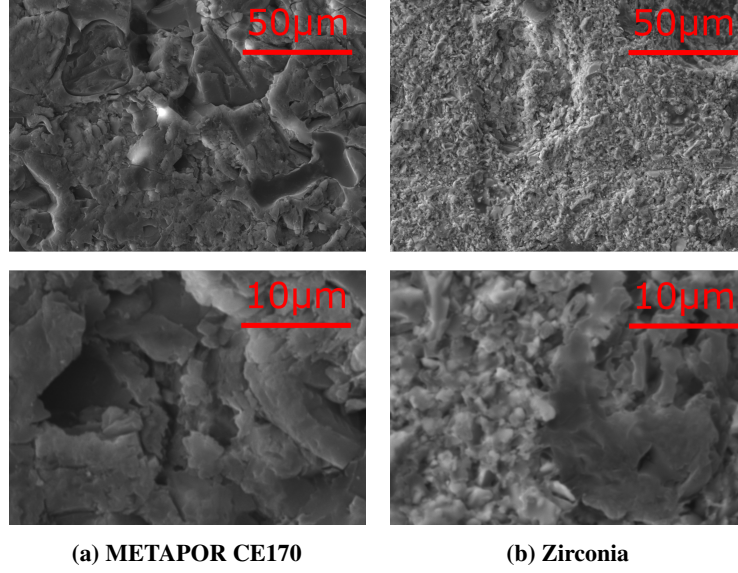


Fig. 3 Microscopic images of the porous injectors at different magnification factors

Table 1 Properties of porous Zirconia (ZrO_2), METAPOR CE170 and PEEK. The thermal properties (ρ, c_p, k) were measured by Netzsch Instruments and the emissivity, ε , was measured using an in-house benchtop setup.

Parameter	ZrO ₂	METAPOR CE170	PEEK
Thickness, L / mm	7	7	10
Porosity, ϕ	0.40	0.20	-
Density, ρ_s / kg m ⁻³	3140	1710	1310
Thermal Conductivity, k_s / W m ⁻¹ K ⁻¹	0.556	1.662	0.25
Specific Heat Capacity, $c_{p,s}$ / J kg ⁻¹ K ⁻¹	462	1177	1201
Thermal Effusivity, $(\sqrt{\rho c_p k})$ / Jm ⁻² K ⁻¹ s ^{-0.5}	1039	1565	627
Darcy Coefficient, K_D / m ²	$1.60 \cdot 10^{-14}$	$2.51 \cdot 10^{-13}$	-
Forchheimer Coefficient, K_F / m	$1.98 \cdot 10^{-10}$	$1.08 \cdot 10^{-8}$	-
Emissivity, ε	0.93	0.95	0.93

The permeability of the samples were measured using an ISO 4022 standard test rig pre and post-experiment according to the procedure detailed in Ifti et al. [7]. The outflow distribution of the employed porous injectors was characterised by hot-wire anemometry with air injection. Due to the large differences in absolute outflow velocities between the two injectors, the obtained normalised velocity maps are shown in Fig. 4. The normalisation is conducted by dividing the velocity at each point against the mean value over the entire porous surface. The resultant span and stream-wise averages are shown in Fig. 5. Porous Zirconia exhibited a predominantly uniform outflow with some local densification towards the bottom right of the injector whilst highly localised jets and regions with almost no outflow were present on the METAPOR CE170 surface. Further comments regarding the permeability distributions of both injectors and the implication to experimental results are explored in Section IV.

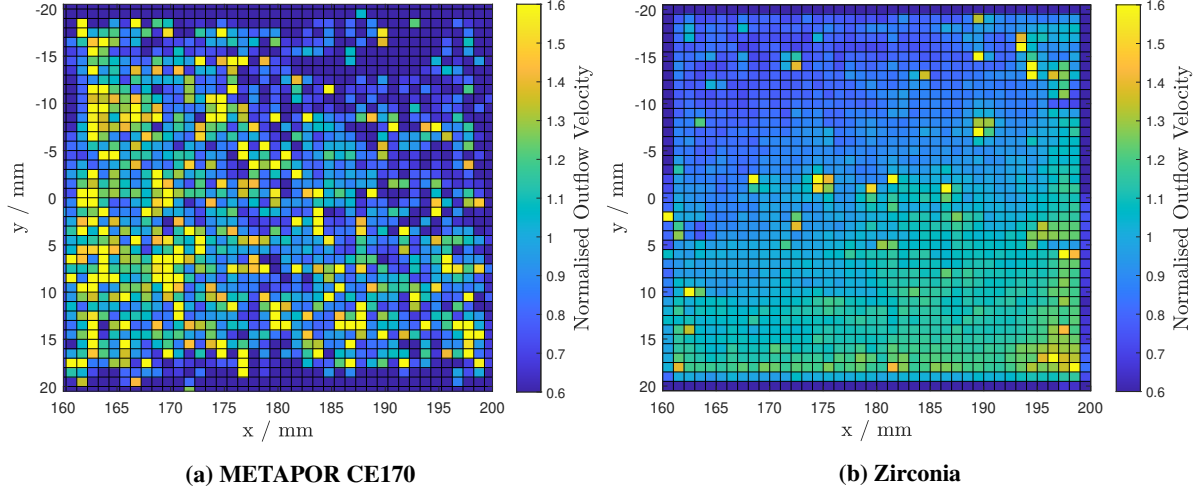


Fig. 4 Outflow velocity maps normalised with the average flow velocity across the injector at 3 bar differential pressure. This was measured with a hot wire with no cross flow. The x and y coordinates correspond to the distance from the leading edge and the distance from the model centre-line respectively.

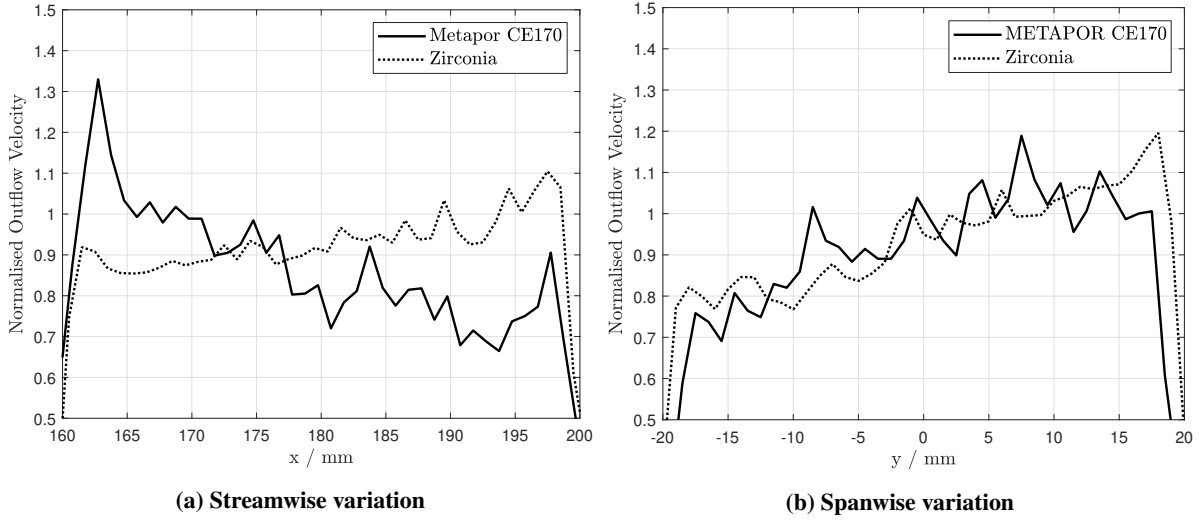


Fig. 5 Span and stream-wise average outflow velocities for Zirconia and Metapor CE170 from the hot wire measurements.

C. Heat transfer measurements

The surface heat flux was primarily measured by employing infrared thermography with additional individual thin film gauges to support and validate the infrared measurements. Infrared thermography spatially resolves the 2D flow structures at the wall and crucially, the non-intrusive [23, 24] nature of this technique permits measurements directly on the porous injector without impeding or otherwise disturbing the coolant outflow. A series of calibration steps, further detailed in Ref. [10], were followed to obtain quantitative transient temperature maps of the flat plate surface including

the transpiration cooled injector from the raw infrared signal.

- 1) Multipoint calibration: Firstly, a multipoint calibration was carried out in-situ using a black body calibrator (CI-Systems SR-33-7 infrared calibrator) to relate the camera raw signal to the true black body temperature inside the wind tunnel test section. This step calibrates the camera and optical system by and spatial non-uniformities or offsets due to the detector or the wider optical system.
- 2) Emissivity measurement: Secondly, to relate the black body temperature to the true material temperature, a material emissivity measurement was performed pre-experiment by using a bench-top setup. The measured emissivity values for both porous injectors and the PEEK surface upstream and downstream of the injector are recorded in Table 1. For these experiments, the directional dependence of emissivity was not required as the maximum angle between camera and the perpendicular to the flat plate surface was 20° wherein the emissivity is roughly constant [25].
- 3) Image Processing: Finally, the images were spatially transformed to a rectangle that represents the physical geometry and passed through an image stabilisation algorithm prior to final post-processing.

After the corrected temperature profile, ΔT , was obtained the heat flux, \dot{q}_w , was determined by applying the impulse response method of Oldfield [26]. A fully coupled transpiration-cooled impulse response method such as in Hermann et al. [27] is not required as the convective heat transfer process between the coolant fluid and porous solid was accounted for by a separate calibration procedure as detailed in Ref. [10]. The thermal product for the porous injector and the downstream PEEK surface is detailed in Table 1. The impulse response is calculated with the assumption that the material thermal response is one-dimensional and semi-infinite. According to Schultz and Jones [28], this assumption is valid as long as the thermal penetration depth is shorter than the thickness of the material. Over a time period of 0.5 s, the penetration depth for METAPOR CE170, Zirconia and PEEK is 2.6, 1.7 and 1.3 mm respectively. These values are all below the recorded the values of material thickness given in Table 1.

Finally, the Stanton number was found by applying the boundary layer edge flow properties as follows

$$St = \frac{\dot{q}_c}{\rho_e u_e c_p (T_r - T_w)} \quad (8)$$

where \dot{q} is the convective heat flux, ρ_e is the freestream density, u_e is the freestream velocity, c_p is the specific heat capacity at constant pressure, T_r is the recovery temperature and T_w is the wall temperature. The recovery temperature is found as per

$$T_r = T_e \left[1 + r \left(\frac{\gamma - 1}{2} \right) M_e^2 \right] \quad (9)$$

where γ is the ratio of specific heats, and r is the recovery factor where $r = \sqrt{Pr}$ for laminar flows and $r = 0.89$ for turbulent flows. Figure 6 shows infrared images from both the LWIR and MWIR cameras for Helium injection onto

laminar flow. The LWIR captures a wide field of view of the flat plate whilst the MWIR images the porous injector only with a greater resolution on the surface. Due to the spectral emissivity dependence of Zirconia detailed above, MWIR images are only presented for the METAPOR CE170 injector.

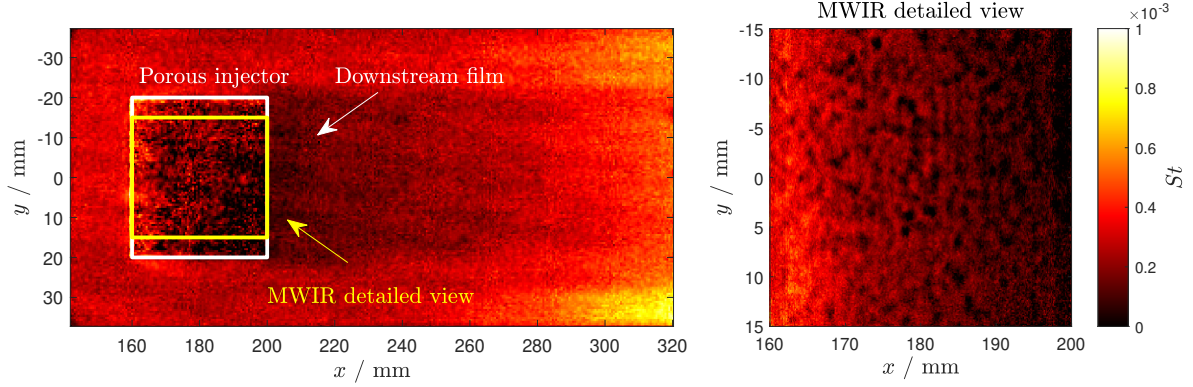


Fig. 6 Illustration of the processed infrared images captured by the two cameras. The presented contours represent Helium injection on the METAPOR CE170 injector at $F = 0.028\%$ at laminar conditions. The LWIR camera has a pixel density of 2 pixels/mm and the MWIR image which focuses on the porous injector has a pixel density of 7 pixels/mm.

D. Flow Conditions

The experiments were conducted in the Oxford High Density Tunnel (HDT) at the Oxford Thermofluids Institute operated in Ludweig tube mode. A detailed description of the facility may be found in [29, 30]. The Mach 6 nozzle was selected and two different freestream conditions were chosen to achieve laminar and turbulent boundary layer states on the model surface. The freestream properties are calculated from measured stagnation pressures upstream of the nozzle throat, pitot pressures, and temperatures using isentropic relations. This is justified as the value of the viscous interaction parameter, $\bar{\chi}$, at $x = 140$ mm (the furthest upstream measurement point), is below 0.18, i.e. viscous effects are negligible [31]. The viscosity was determined using Keyes model [32] and Table 2 presents an overview of the flow conditions. The total test time for each individual experimental point was approximately 30 ms.

Table 2 Freestream flow conditions

Parameter	Laminar	Turbulent
Pressure, p_∞ / Pa	786	1737
Temperature, T_∞ / K	49.6	42.6
Velocity, u_∞ / m s ⁻¹	861	798
Density, ρ_∞ / kg m ⁻³	0.0548	0.142
Mach number, M_∞	6.1	6.1
Unit Reynolds number, Re_u / m ⁻¹	$13.3 \cdot 10^6$	$37.2 \cdot 10^6$
Estimated boundary layer height, δ_{99} / mm at $x = 160$ mm	2.36	4.44

The blowing ratio, F (Eq. (4)), is determined from the measured plenum and freestream pressures and temperatures according to the Darcy-Forchheimer equation [33]

$$\frac{p_f^2 - p_e^2}{2LR_fT_f} = \frac{\mu_f \rho_f u_f}{K_D} + \frac{(\rho_f u_f)^2}{K_F} \quad (10)$$

where the values of the permeability coefficients, K_D and K_F are given in Table 1. For the blowing parameter (Eq. (3)), St_0 is the experimentally measured Stanton number when $F = 0$. Table 3 presents an overview of all the cases considered in this study.

Table 3 Overview of blowing cases at both laminar and turbulent conditions (Table 2). Note: The value of blowing parameter requires St_0 and has thus been calculated based on the surface heat transfer without injection for the laminar and turbulent cases respectively.

Parameter	Laminar				Turbulent		
Injector	METAPOR CE170		Zirconia		METAPOR CE170		Zirconia
Coolant gas	N ₂	He	N ₂	He	N ₂	He	N ₂
Mass flux, $\rho_f u_f$ / kg m ⁻³	0.012-0.081	0.0071-0.013	0.0078-0.032	0.0050	0.049-0.30	0.017-0.027	0.021-0.046
Blowing ratio, F / %	0.026-0.17	0.015-0.028	0.016-0.067	0.011	0.043-0.26	0.015-0.024	0.019-0.040
Blowing Parameter, B_h	0.99-6.45	0.57-1.06	0.63-2.60	0.406	0.65-3.78	0.18-0.36	0.26-0.56

IV. Results

For both the laminar and turbulent cases described in Table 2, it was first necessary to ascertain that the correct boundary layer state was achieved without blowing. This was confirmed by measuring the surface heat flux and comparing to the values to Eckert's heat flux correlations for laminar and turbulent boundary layers on a flat plate [34]. Figure 7 shows the span-wise averaged line plots between $y = -15$ mm and $y = 15$ mm for the two conditions. Both the laminar and turbulent cases match well with the Eckert curves and the individual thin film gauges on and upstream of the porous injector. For the laminar case, it is clear that the boundary layer then transitions at approximately $x = 205$ mm to the turbulent level after 320 mm. This is satisfactory as the primary purpose of these experiments are to present heat transfer measurements purely on the porous injector region. Later in Section IV.D, the downstream results will be presented only for the turbulent cases. Estimated boundary layer thicknesses at the start of the porous injector ($x = 160$ mm) are recorded in Table 2. The values are estimated by assuming a Blasius boundary layer profile for both the laminar and turbulent cases [35]. Compressibility is accounted for by calculating the Reynolds number based on the reference temperature [34]. It must be noted that the estimate for the turbulent boundary layer assumes that the flow is fully turbulent from the start of the flat plate. This is not true for these experiments (turbulence is incited by a boundary layer trip) and therefore the quoted boundary layer thickness for the turbulent case is likely to be an overestimate.

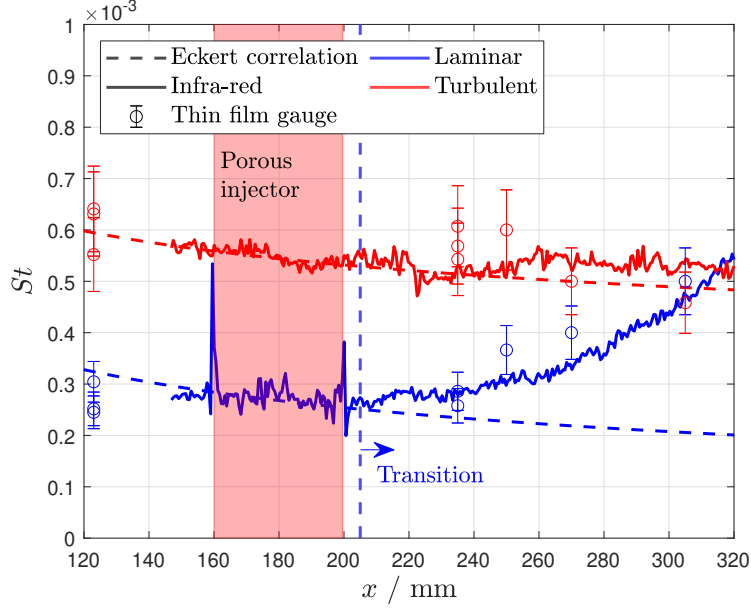


Fig. 7 Comparison of measured Stanton numbers with the Eckert laminar and turbulent correlations [34]. The span-wise average is taken between $y = -15$ mm and $y = 15$ mm.

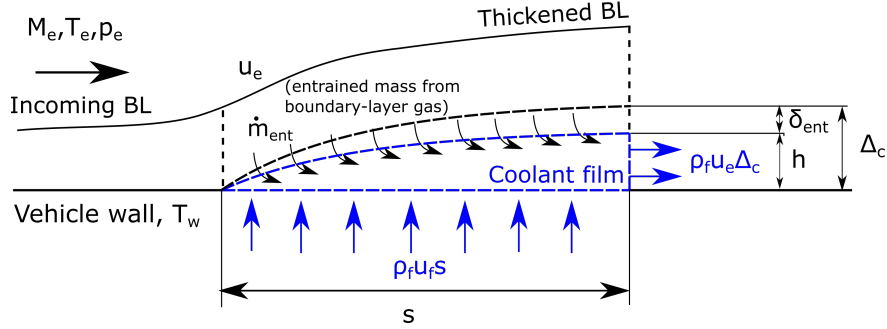


Fig. 8 Control volume around the injected gas and the mass entrainment into the coolant gas over the injector. Adapted from Ifti [36]; reprinted by permission of the authors

It is well established by previous studies [18, 37] that the introduction of the coolant layer thickens the incoming boundary layer. The height of the coolant sub-layer be modelled by considering the continuity equation across a simple control volume as presented in Fig. 8. As detailed by Ifti [36], by assuming that the coolant is at the same temperature as the vehicle wall, T_w , and that the coolant reaches the edge velocity, u_e , after becoming tangential to the wall; the resultant height of the coolant layer at the end of the injector is

$$\Delta_c = h + \delta_{ent} \quad (11)$$

where

$$h = \frac{M_e T_w}{M_f T_e} F s \quad (12)$$

and δ_{ent} , which is the growth of the coolant layer due to the entrained boundary layer gas. s in Eq.11 is the stream-wise length of the porous injector. δ_{ent} is approximated as a Blasius laminar or turbulent boundary layer thickness solutions (depending on whether this analysis is undertaken for a laminar or turbulent boundary layer) beginning at the injector's starting point. Figure 9 shows the variation in Δ_c for the experimentally tested conditions with blowing ratio. Due to the approximately seven times smaller molecular weight of Helium compared to Nitrogen, there is a corresponding change in the coolant layer height due to injection for a given blowing ratio. In the following sections, the effect of blowing to the surface heat transfer at both laminar and turbulent conditions are examined in detail.

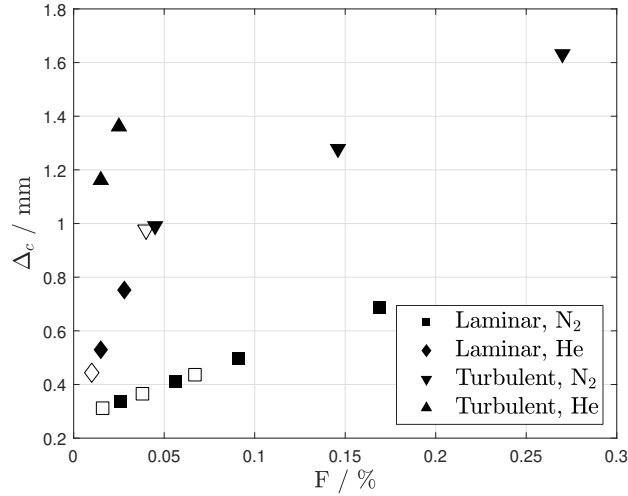


Fig. 9 Estimated change in the coolant layer height, Δ_c , with blowing ratio for the experimentally tested laminar and turbulent conditions. The filled points refer to conditions tested using the METAPOR CE170 injector and the unfilled points for the Zirconia injector.

A. Laminar flow on injector

Several different blowing ratios were tested for the METAPOR CE170 and Zirconia injectors with both Nitrogen and Helium coolant gases. An overview of these cases are presented in Table 3. Relatively low blowing ratios were selected to ensure that the flow remains laminar along the injector; previous studies by Tanno et al. [38] have shown that at high blowing ratios, injection may lead to early transition. Contour plots of the surface Stanton reduction (St/St_0) on the porous injector are presented in Fig. 10 for a subset of blowing cases where both the METPAOR CE170 and Zirconia injectors have similar blowing ratios. The introduction of the low-momentum coolant into the sublayer of the boundary layer can significantly reduce the temperature and velocity gradients close to and at the wall. This is demonstrated in Fig. 10 where both the Nitrogen and Helium injection cases exhibit a gradual decrease in Stanton number reduction downstream from the start of the injector. Both injectors show similar trends with a generally uniform, 2D heat transfer

distribution even for the highly non-uniform METAPOR CE170 injector.

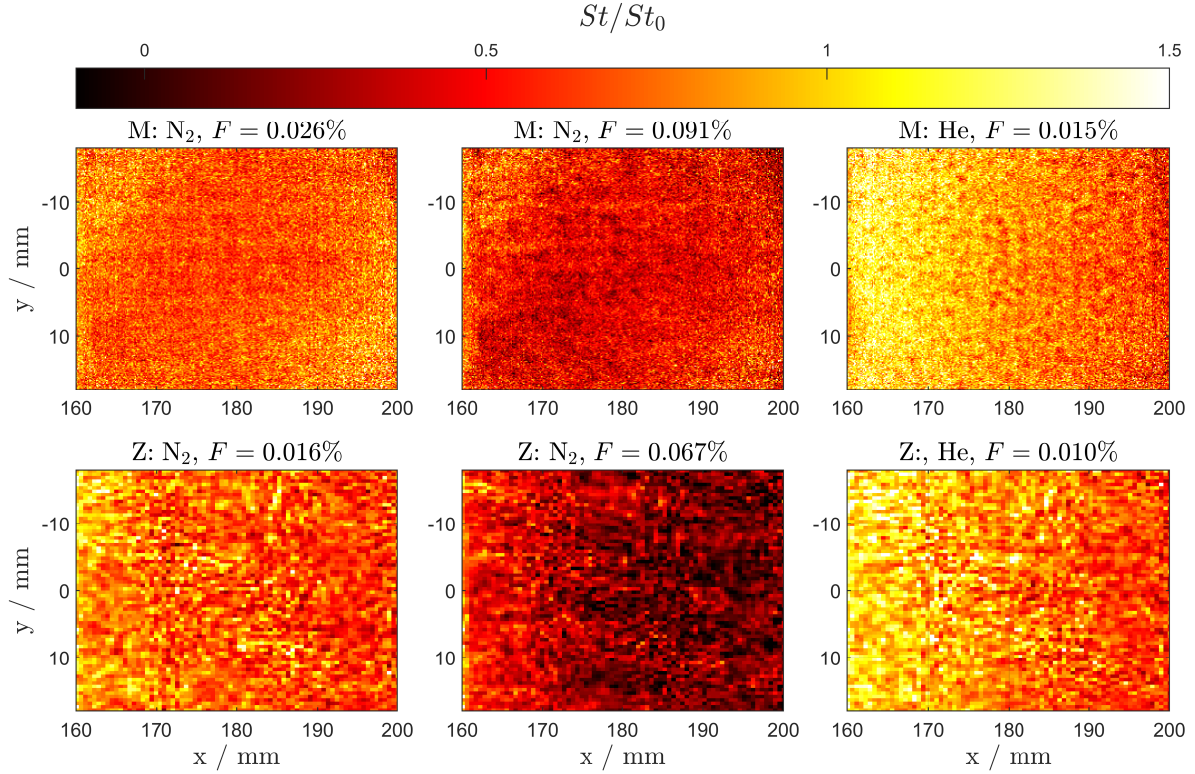


Fig. 10 Comparison between the METAPOR CE170 and Zirconia injector for the laminar condition. Note: the Zirconia images have lower resolution due to the FLIR camera. M represents the METAPOR CE170 injector and Z the Zirconia.

The span-wise averaged values of the Stanton number reduction are plotted versus the stream-wise direction, x , in Fig. 11. As the blowing ratio, F , increases the Stanton number reduces, reaching essentially zero for the highest Nitrogen injection case. The rise in the experimental points at around $x = 170$ mm for Nitrogen injection with the METAPOR CE170 injector may be due to either the non-uniformity of the porous injector or perhaps a sign of earlier transition than expected. Whilst Nitrogen injection gives a very uniform coverage over the porous sample, the Helium cases show an initial heat flux augmentation at $x \approx 160$ - 162 mm and thereafter a very steep drop towards the end of the injector. The initial increase in surface heat flux is likely due to the fact that at the very start of the injector, the wall temperature gradient does not change significantly due to the inclusion of Helium injection. However, due to the high concentration of Helium at the wall, the effective mixture thermal conductivity at the wall is higher than the free-stream air. Thus, it is possible for a higher resulting heat flux close to the interface between the injector and the wall with blowing than the wall heat flux without injection.

It is notable that at the end of the injector ($x = 195$ mm), a Helium blowing ratio of 0.028% achieves a comparable level of cooling to Nitrogen at 0.091% - over a factor of three times larger. This is consistent with the findings from

other experiments [39] where Helium was found to be significantly more effective in terms of heat transfer reduction compared to Nitrogen due to both its higher specific heat capacity and lower molecular weight. The lower molecular weight of Helium means that a higher plenum pressure is needed for a given mass flux through the injector. Thus both Helium exits at a higher velocity due to its lower density and, in addition, there is a larger volume of Helium at exit.

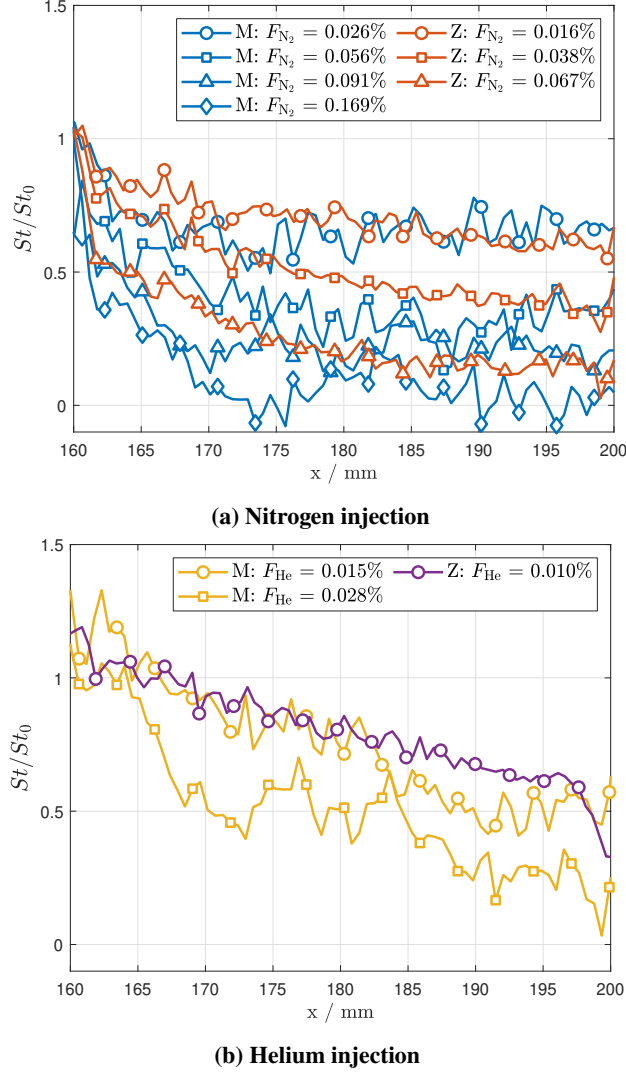


Fig. 11 Span-wise averaged Stanton number reduction along the porous injector at the laminar condition. The average is taken between $y = -15$ mm and 15 mm assuming a two-dimensional injector. M represents the METAPOR CE170 injector and Z the Zirconia.

B. Turbulent flow on injector

Figure 12 shows contours of Stanton number reduction for different Nitrogen and Helium blowing ratios for both the Zirconia and METAPOR CE170 injectors. For Nitrogen injection, similar to the laminar cases, both injectors exhibit a very uniform heat transfer distribution on the surface. Compared to the laminar cases, there is little visible

change in Stanton number reduction along the sample. For high blowing ratios ($F = 0.27\%$), a region of heat transfer enhancement is present at the beginning of the injector ($x = 165\text{-}175\text{ mm}$) before a gradual reduction downstream. A highly non-uniform distribution is exhibited by the Helium case with the individual 'cold' spots akin to the hot wire map in Fig. 4.

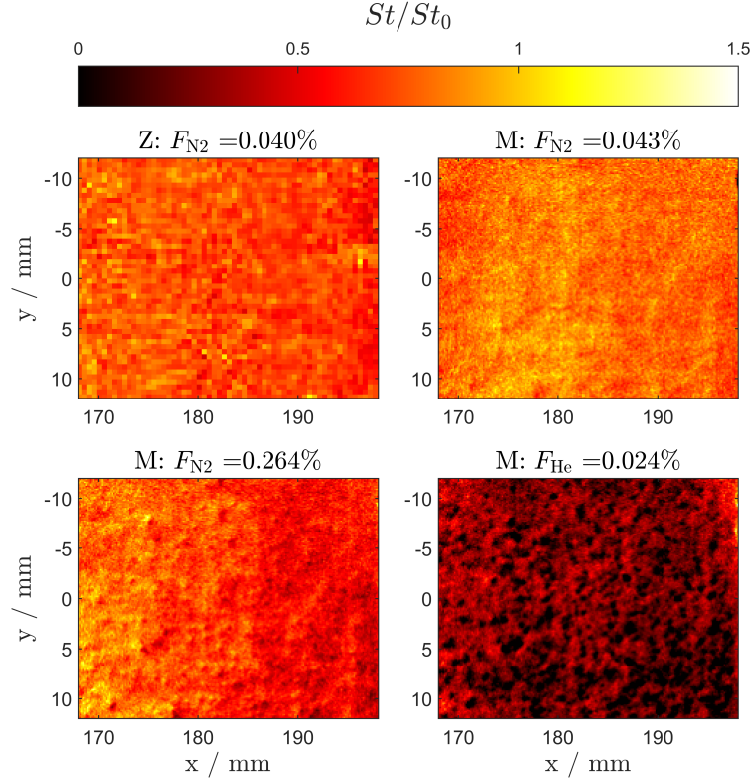


Fig. 12 Comparison between the METAPOR 170CE and Zirconia injector for the turbulent condition. Note: the Zirconia images have lower resolution due to the FLIR camera. M represents the METAPOR CE170 injector and Z the Zirconia

Figure 13 depicts span-wise averaged values of the Stanton number reduction versus the stream-wise direction, x . As the the blowing ratio, F , increases the Stanton number reduces. The profiles are fairly flat with little variation with stream-wise direction after around $x = 170\text{ mm}$. For Nitrogen injection, as the blowing ratio increases, there is an increase in Stanton number over the uncooled case at the beginning of the injector (see inset Fig. 13). This suggests that, for turbulent flow, the compression shock formed by the thickening of the boundary layer increases in strength with higher blowing ratio and gives rise to up to 40% promotion in Stanton number for the highest blowing case. Both the METAPOR CE170 and Zirconia injectors behave similarly with the same flat Stanton reduction profiles at comparable blowing ratios. There is a marked reduction for even very low blowing ratios of Helium injection. For a blowing ratio of 0.25%, the surface Stanton number with Nitrogen is roughly 40% of the uncooled case at the end of the porous injector whilst for Helium only a blowing ratio of 0.015% is required for a comparative heat reduction. The substantial heat

reduction due to Helium is well beyond expected values based on known correlations for turbulent flows [40].

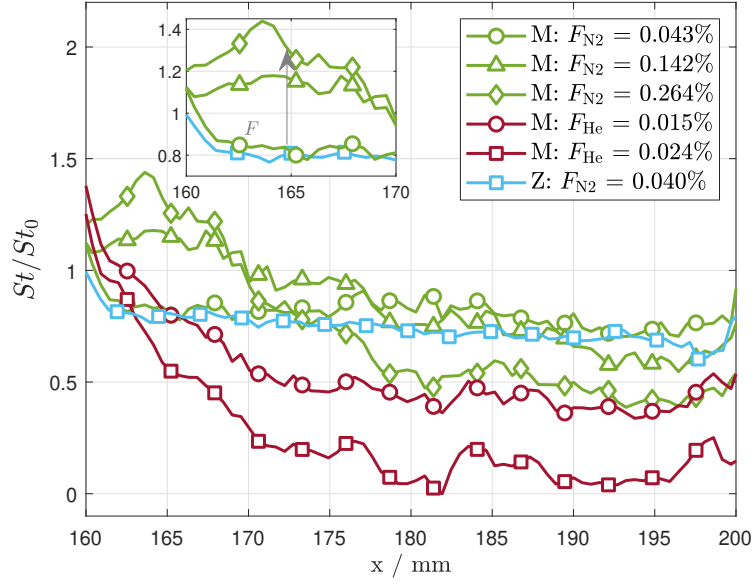


Fig. 13 Span-wise averaged Stanton number reduction along the porous injector at the turbulent condition. M represents the METAPOR CE170 injector and Z the Zirconia. The average is taken between $y = -15$ mm and $y = 15$ mm assuming a two-dimensional injector.

C. Correlations

In previous works [11, 12], the heat transfer reduction across different blowing ratios and coolants were correlated against the blowing parameter, B_h , by employing one of either Eq. (2) or (5) for laminar or turbulent flows respectively. Figure 14 shows the experimental blowing parameters at each stream-wise axial location on the injector plotted against the span-wise average Stanton number reduction for both the laminar and turbulent cases. Each data point represents the span-wise average over a particular location x , i.e. on a pixel row. Whilst there is a clear trend of increased cooling with higher blowing parameter and there is an intersection between the theoretical curves of Mickley and Moyer-Rindal, especially for the laminar cases, the stream-wise heat transfer distribution on the injector is not captured. This is because St_0 does not change appreciably over the length of the injector and F is a single value for the constant mass injection cases presented in this study.

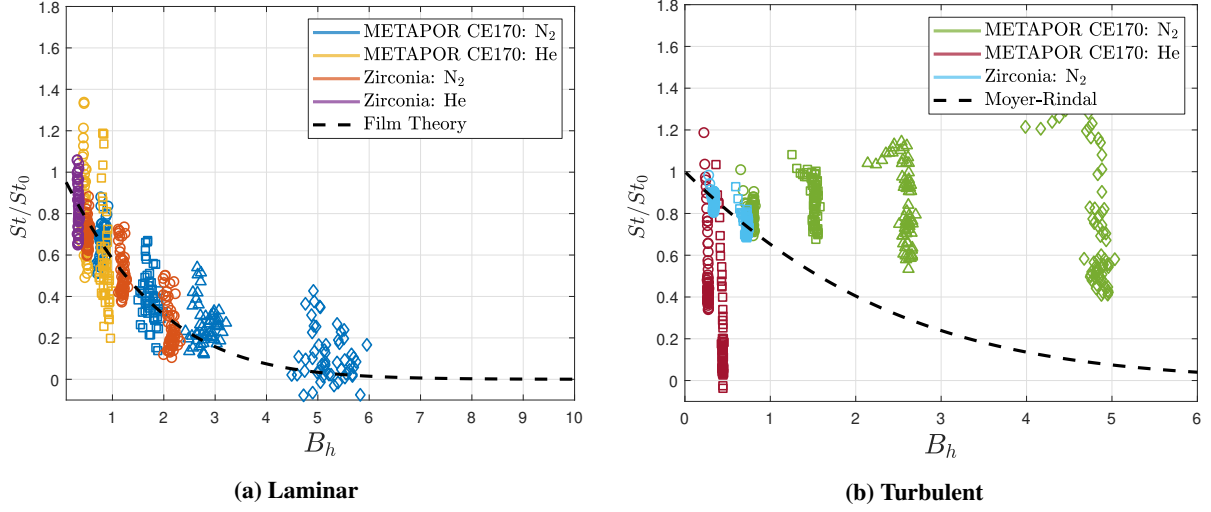


Fig. 14 Span-wise averaged Stanton reduction between $y = 15$ to -15 mm on the porous injector against the blowing parameter, B_h (based on the local St_0 at each location) for all injection cases.

Clearly, the influence of the injector needs to be accounted for to capture the axial variation in heat transfer on the injector. For this purpose a correction to account for the boundary layer development as shown in Eqs. (6) and (7) may be applied to the experimental data points. Figure 15 shows all the experimental data points plotted for both laminar and turbulent conditions. Whilst good agreement is observed for the laminar cases with Nitrogen injection and turbulent with low Nitrogen injection, the other cases all exhibit a divergence from the correlation. This is because one of the inherent assumptions of this model is that when $x = x_s$, the value of $St/St_0 = 1$; i.e. any cooling begins at the exact start of the injector. However, this may not always be true for all cases, especially for high blowing cases where the boundary layer may grow slightly upstream of the injector or if, like in the turbulent cases, there is a region of heat flux enhancement near the start of the injector. The proposed correlation parameters do not capture the complex interaction between the coolant outflow and the incoming boundary layer at the very start of the injector but, rather, predict the evolution from an initial point. For this reason, to correlate the experimental data points, the modified correlation parameter may be plotted not against St/St_0 but rather against $\frac{St/St_0}{(St/St_0)_{\max}}$, i.e. normalised against the peak value of St/St_0 . The chosen $(St/St_0)_{\max}$ values are the cyan filled symbols in Fig. 15. Generally speaking, this occurs at start of the injector, x_s , but may also be a few mm downstream as is the case for the higher blowing turbulent cases with Nitrogen injection (Fig. 13).

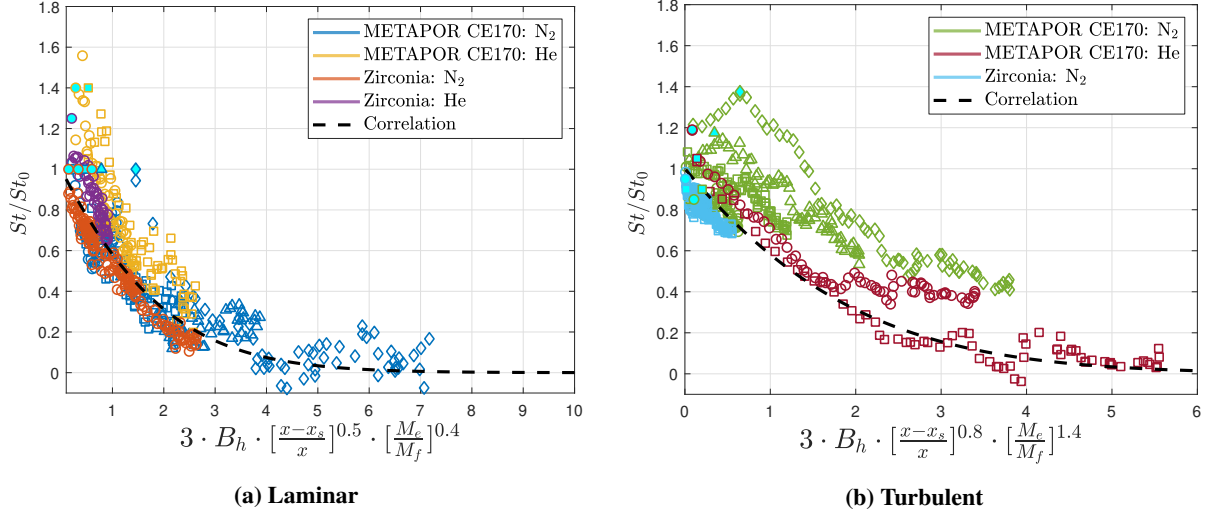


Fig. 15 Span-wise averaged Stanton reduction between $y = 15$ to -15 mm on the porous injector against the blowing parameter, B_h (based on the local St_0 at each location) for all injection cases. Correlation refers to Eqs (6) and (7). The filled cyan points are selected values of $(St/St_0)_{\max}$ for each case.

Figure 16 shows the same experimental points as above but with the x axis replaced with λ and ω from Eqs. (6) and (7) as well as the y axis replaced with $\frac{St/St_0}{(St/St_0)_{\max}}$ as discussed above. To achieve a good fit with experimental data a value of $C = 3$ and $m = 0.4$ for the laminar cases and $D = 3$ and $n = 1.4$ for the turbulent cases was chosen. Overall, both correlations reasonably capture the effect of the injected mass flux, the growth of the boundary layer at the injector and the differences in molecular properties of the Nitrogen and Helium coolants. Whilst C and D are purely empirically derived factors for the present freestream test conditions, there is a greater significance to the chosen value of the exponents m and n . For the laminar case, the value of $m = 0.4$ is also referenced by Marvin and Pope [14] as an upper bound correction factor to account for differing fluid properties between the injected and freestream gas in laminar stagnation point flows. For the turbulent cases, several values for the exponent between 0.5 and 1 have been stated depending on the experimental data [6, 41]. An exponent of 1.4 is higher than expected, suggesting that Helium injection is a more effective coolant in turbulent flows than previously observed for these freestream conditions and geometry. In fact, the factor $\left(\frac{M_e}{M_f}\right)^{1.4}$ translates to Helium possessing 16 times the cooling effectiveness of an equivalent blowing parameter of Nitrogen. However, it must be stressed that this is based on only two Helium injection cases and further experimental and computational studies are required to fully understand this effect.

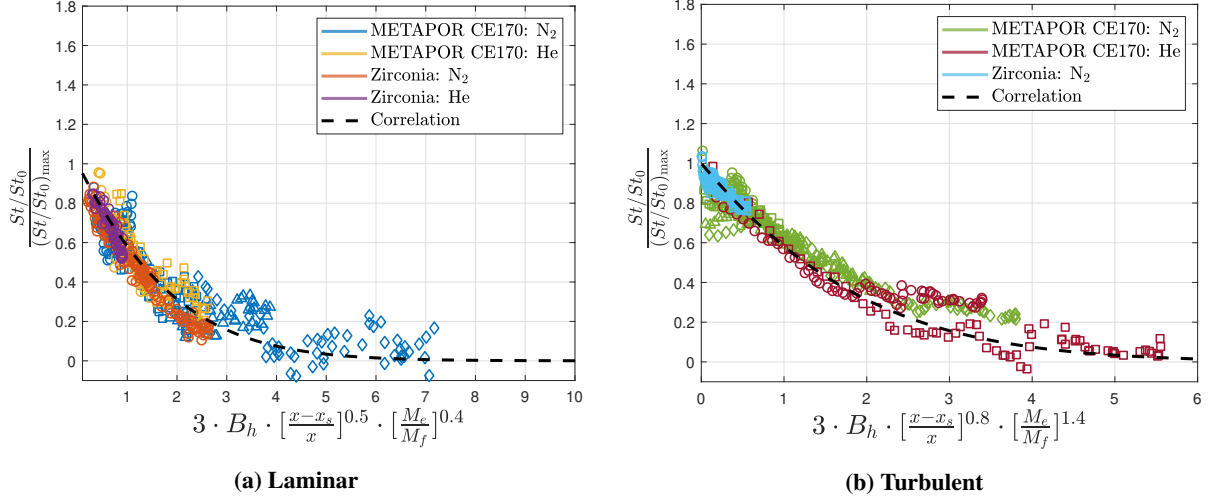


Fig. 16 Span-wise averaged $\frac{St/St_0}{(St/St_0)_{\max}}$ between $y = 15$ to -15 mm on the porous injector against the correlation factors in Eqs (6) and (7) for all cases. Correlation refers to Eqs (6) and (7)

Figure 17 show both correlations applied to a subset of span-wise averaged experimental data points. For the laminar cases, an extremely good fit within 5% of the experimental data is attained for the Zirconia injector for both the Nitrogen and Helium injection cases. This material, as demonstrated above produces an extremely uniform outflow, closely resembling the assumed uniform mass injection boundary condition. Greater scatter with up to 30% deviation is present for the METAPOR CE170 cases even though the trend is consistent with zirconia. The sharp local variations present for all the cases with this injector highlight the importance of selecting an injector with a uniform outflow to ensure that all regions on the surface are cooled to the required degree. A similar level of agreement is seen for the turbulent cases wherein, with Nitrogen injection, the correlation lies within 10% of the experimental points when the correlation curves are set to begin at the point of maximum heat transfer at $x = 164$ mm. For the Helium case presented, whilst the correlation follows the general trend, there is greater scatter in the experimental curve and the correlation under-predicts the heat transfer reduction, especially from $x = 160$ to 182 mm.

Overall, the presented correlation parameters correctly capture the axial heat transfer distribution at the start of a finite length porous injector for both laminar and turbulent cases. In particular, this shows that in certain scenarios, it may be more beneficial to begin the transpiration cooled wall upstream of a predicted high heat flux region than to inject at higher mass fluxes so that the film is fully developed by the time it arrives at that region.

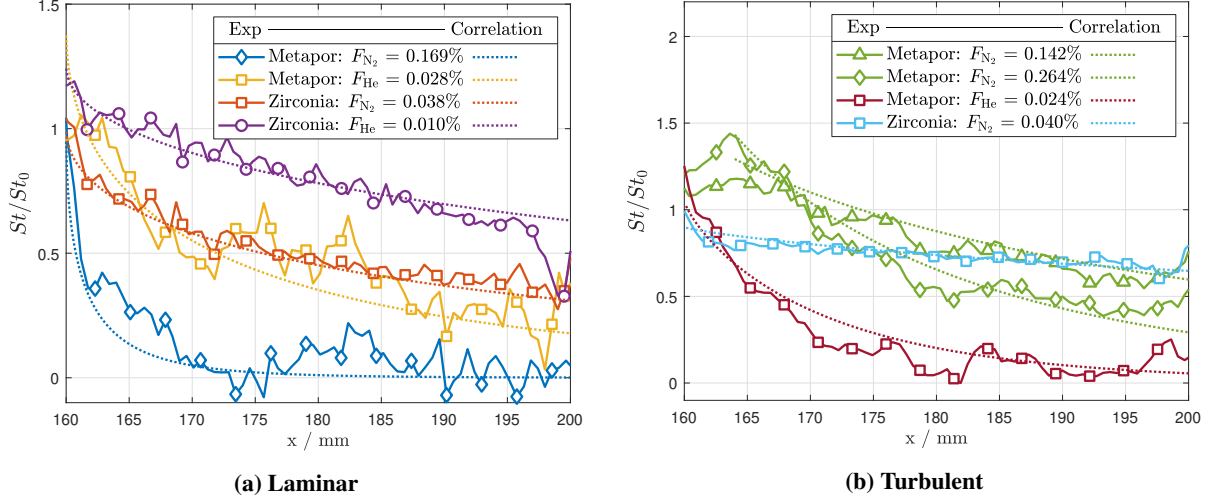


Fig. 17 Comparison between the span-wise averaged experimental heat transfer reduction and predicted by the correlations in Eqs (6) and (7).

D. Turbulent Downstream effectiveness

As noted previously, for the laminar cases, transition began right after the end of the porous injector and thus it is not possible to comment on the effectiveness of injection as it mixes downstream with the external boundary layer for laminar flows. Several studies have been completed on this topic for slot injectors [15, 16, 42] and more recently, Ifiti et al. [20], characterised the downstream laminar effectiveness for Mach 7 flows on the same experimental model as this paper. However, as indicated by Fig 7, for the turbulent case, the boundary layer was fully turbulent up to the end of the field of view of the infrared camera and thus the downstream mixing may be examined for different blowing rates and for Nitrogen and Helium injection.

To compare with existing literature [16], the heat flux reduction can also be formulated as an isothermal cooling effectiveness

$$\eta_{th} = 1 - \frac{St}{St_0}, \quad (13)$$

where the subscript '0' denotes the uncooled case. A case of 100% cooling, i.e. zero Stanton number to the wall, would result in an effectiveness of 1. Contour plots of the thermal effectiveness are plotted in Fig. 18 for the highest injection cases using Nitrogen and Helium respectively. Whilst both cases have a similar trend of diminishing effectiveness as the coolant mixes further downstream, it is notable that for the highest Nitrogen injection, the coolant film diffuses laterally and is wider than the span of the injector. As per Fig. 4 and 5, there is significant non-uniformity in the METAPOR CE170 injector with greater outflow at the bottom half of the injector ($y < 0$ mm) compared to the top half. The averaged normalised outflow velocity for the top half of the injector is 55% of the whole injector compared to 45%

at the bottom. The asymmetric outflow is present in the downstream film with greater coverage between 10 and 20 mm compared to -10 and -20 mm displaying fully three-dimensional behaviour. However, as the film convects downstream, the 3D nature of the film close to the injector gradually reduces as the film mixes with the hypersonic crossflow at higher rates downstream until the film is almost totally uniform in the span-wise direction. Similar observations have been noted by Ifti et al [19].

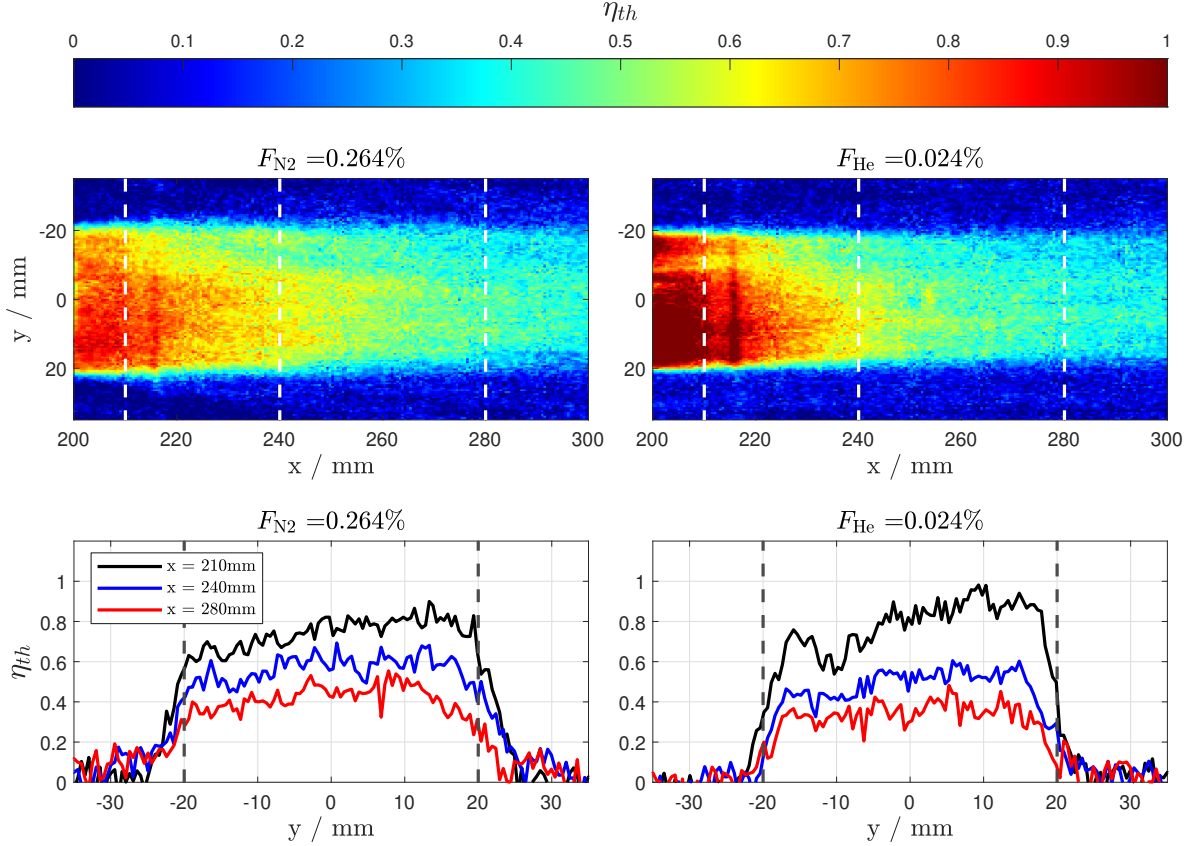


Fig. 18 Contour plots of downstream isothermal efficiency for the highest Nitrogen and Helium injection cases in turbulent flow with the METAPOR CE170 injector. The three span-wise slices are taken at $x = 210, 240$ and 280 mm.

Furthermore, Fig. 19 shows the span-wise average thermal efficiencies from the end of the injector ($x = 200$ mm) to 310 mm from the leading edge. All of the cases exhibit a similar, close to linear, monotonic trend of reduced thermal efficiency as the coolant traverses further downstream. Essentially, with increased blowing ratio, i.e. coolant mass flux, the film coverage improves on the injector as well as downstream. For low Nitrogen blowing ratios, there is little reduction in the thermal efficiency as the film convects downstream, i.e. the gradient is very shallow. The coolant film retains a baseline level of thermal efficiency even at $x = 300$ mm with a drop from 0.08 to 0.05 for $F_{N_2} = 0.040\%$. In contrast, the highest Nitrogen injection cases display a very steep drop off from an efficiency of almost 1.0 at the end of the injector for $F_{N_2} = 0.264\%$ to 0.3 just 100 mm downstream. For Helium injection, the trend is slightly dissimilar

to Nitrogen with a marginally steeper gradient. This is expected due to the higher volume and different molecular properties of the Helium film.

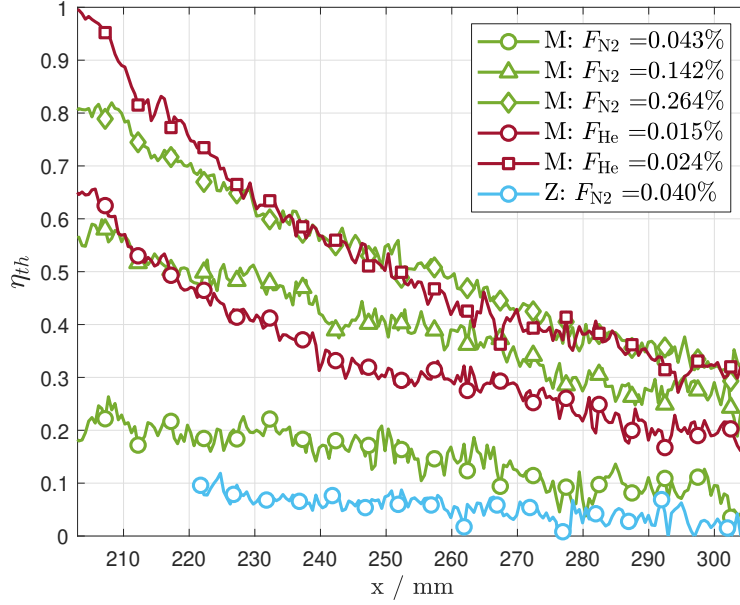


Fig. 19 Span-wise average thermal efficiencies from the end of the injector to 310 mm from the leading edge. **M** represents the METAPOR CE170 injector and **Z** the Zirconia injector. The spanwise averages are taken from $y = -15$ to 15 mm.

The obtained values of η may be correlated by a factor defined by Homsbsch (using the same approach as Goldstein [16]):

$$\xi = \left(\frac{C^*}{Re_u} \right)^{0.2} \left(\frac{T_e}{T^*} \right)^{0.6} \frac{x'^{0.8}}{F \cdot s} \quad (14)$$

where x' is the distance from the start of the injector, C^* is the Chapman-Rubesin factor evaluated at Eckert's reference temperature $((T_e/T^*)(\mu^*/\mu_e))$, and s is the stream-wise length of the injector. Whilst this correlation factor is strictly speaking for when the injected gas is the same as the freestream, a scaling factor of $(c_{p,f}/c_{p,e})^{1.4}$ is used to account for the Helium cases. This factor essentially translates to a factor of 10 which is in between the factor $(M_e/M_f)^{0.4}$ for laminar flow over the injector and $(M_e/M_f)^{1.4}$ for turbulent referred to by the correlations above (Fig. 17). The fact that the dissimilar gas correlation factor varies between on and downstream of the injector and for different flow conditions reinforces the fact that a more complex physical model is required to accurately capture the effect of dissimilar gases across different flow scenarios.

Homsbsch [16] proposed the following correlation for turbulent cases:

$$\eta_{th} = \begin{cases} 1 & \text{for } \xi \leq 1.85, \\ [1 + 0.32(\xi - 1.85)]^{-0.8} & \text{for } \xi > 1.85, \end{cases} \quad (15)$$

for blowing ratios from 18-53%. For the lower blowing ratios and higher Mach number in this study ($M = 6.1$ and $F = 0.019$ - 0.264%), the following modification to the correlation is proposed

$$\eta_{th} = \begin{cases} 1 & \text{for } \xi \leq 4.5, \\ [1 + 0.15(\xi - 4.5)]^{-0.8} & \text{for } \xi > 4.5. \end{cases} \quad (16)$$

which successfully lines up with the experimental data (Fig. 20). Due to the large difference in blowing ratio between the experiments conducted in Ref. [16] and the present work, it is not surprising that there is a difference between Eqs. (15 and 16). The current data set demonstrates the shortcomings of existing general models of downstream effectiveness for turbulent flows and further experiments at a wider range of conditions will help develop confidence in this model to accurately model these flows.

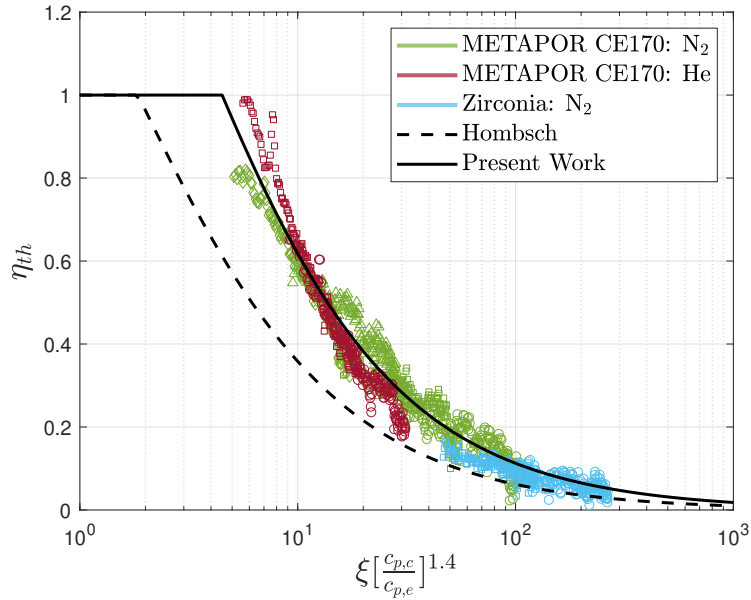


Fig. 20 Thermal effectiveness, η_{th} , verses the correlation factor, ξ . The present work represents Eq (16).

V. Conclusions

In this study, the spatial, two-dimensional, surface heat transfer of two transpiration cooled micro-porous injectors was measured in laminar and turbulent hypersonic flow. It was found that a modification to film theory which accounts for the boundary layer growth at the start of the injector successfully correlates the heat transfer reduction across different blowing rates for Nitrogen and Helium. Injection in the laminar regime results in a steady, monotonic reduction in

heat transfer whilst a much flatter profile was observed in the turbulent regime. Helium was found to be more effective at cooling in both laminar and turbulent flows than reported previously in literature. In the turbulent regime, Helium exhibited a cooling effectiveness 16 times greater than Nitrogen. The outflow uniformity of a porous injector was found to have a great impact on the spatial heat transfer distribution. A uniform outflow leads to consistent coverage of coolant over the injector with no local hot spots.

Overall, the results published add insight to the spatial variation in local heat transfer on the injector surface and how the film build-up differs between laminar and turbulent flows. Whilst the presented correlations are specific to the flow conditions used in these experiments, they may still be used as a preliminary design tool for sizing a transpiration cooled system. Further experimental and numerical studies covering a wider parameter space of free-stream conditions and coolant gases may yield a generalised correlation applicable across a range of flight conditions. In particular, it has been noted in the literature that the blowing parameter does not capture Mach number dependency [43] and further exploration of such parameters to the resultant surface heat transfer on transpiration cooled surfaces will be beneficial for wider applicability of the correlations presented in this work.

VI. Acknowledgements

This research is funded by the EPSRC grant "Transpiration Cooling Systems for Jet Engine Turbines and Hypersonic Flight" (reference: EP/P000878/1). The authors would also like to thank the Reaction Engines and Engineering and Physical Sciences Research Council Collaborative Awards in Science and Engineering reward for supporting the studentship of Imran Naved. The authors are also grateful for the tireless work of Dr Luke Doherty and Mailys Buquet in the operation of the High Density Tunnel. Thanks is also extended to Greg King for his tireless efforts preparing and instrumenting the model ahead of the experiments. Lastly, the authors would like to extend their gratitude toward the reviewers who improved the quality of this paper.

References

- [1] Van Driest, E. R., "Investigation of Laminar Boundary Layer in compressive Fluids Using the Crocco Method," *NACA TN 2597*, 1952.
- [2] Giles, D. N., "Integral cooling system for high-temperature missile structures," , 1988.
- [3] Stalmach, C., Bertin, J., and Pope, T., "A Study of Boundary Layer Transition on Outgassing Cones in Hypersonic Flow," *NASA CR-1908*, 1971.
- [4] Pappas, C., and Lee, G., "Heat transfer and pressure on a hypersonic blunt cone with mass addition," *AIAA Journal*, Vol. 8, No. 5, 1970, pp. 954–956. doi:10.2514/3.5801.

- [5] Langener, T., Wolfersdorf, J. V., and Steelant, J., "Experimental Investigations on Transpiration Cooling for Scramjet Applications Using Different Coolants," *AIAA Journal*, Vol. 49, No. 7, 2011, pp. 1409–1419. doi:10.2514/1.j050698.
- [6] Holden, M. S., and Sweet, S. J., "Studies of transpiration cooling with shock interaction in hypersonic flow," *AIAA 25th Plasmadynamics and Lasers Conference, 1994*, American Institute of Aeronautics and Astronautics Inc, AIAA, 1994. doi:10.2514/6.1994-2475.
- [7] Ifti, H. S., Hermann, T., McGilvray, M., Larrimbe, L., Hedgecock, R., and Vandeperre, L., "Flow Characterisation of Porous Ultra-High-Temperature Ceramics for Transpiration Cooling," *AIAA Journal*, 2022. doi:https://doi.org/10.2514/1.J061009.
- [8] Pappas, C., and Okuno, A. F., "Heat-transfer measurement for binary gas laminar boundary layers with high rates of injection," *NASA TN D-2473*, 1964, pp. 1–45.
- [9] Strauss, F., Witte, J., Weißwange, M., Manfletti, C., and Schlechtriem, S., "Experiments on shock-boundary layer interaction and cooling efficiency in a transpiration cooled model scramjet," *53rd AIAA/SAE/ASEE Joint Propulsion Conference, 2017*, 2017. doi:10.2514/6.2017-4833.
- [10] Naved, I., Hermann, T., McGilvray, M., Ewenz Rocher, M., Hambidge, C., Doherty, L., Le Page, L., Grossmann, M., and Vandeperre, L., "Heat Transfer Measurements of a Transpiration Cooled Stagnation Point in Transient Hypersonic Flow," *Journal of Thermophysics and Heat Transfer*, 2022.
- [11] Mickley, H. S., Ross, R. C., Squyers, A. L., and Stewart, W. E., "Heat, Mass, and Momentum Transfer for Flow Over a Flat Plate With Blowing or Suction," *NACA TN 3208*, 1954.
- [12] Thompson, R. A., and Gnoffo, P. A., "Implementation of a blowing boundary condition in the LAURA code," *46th AIAA Aerospace Sciences Meeting and Exhibit*, American Institute of Aeronautics and Astronautics Inc., 2008. doi:10.2514/6.2008-1243.
- [13] Moyer, C. B., and Rindal, R., "An analysis of the coupled chemically reacting boundary layer and charring ablator. Part 2 - Finite difference solution for the in-depth response of charring materials considering surface chemical and energy balances," *NASA CR-1061*, 1968.
- [14] Marvin, J. G., and Pope, R. B., "Laminar convective heating and ablation in the Mars atmosphere." *AIAA Journal*, Vol. 5, No. 2, 1967, pp. 240–248. doi:10.2514/3.3948.
- [15] Goldstein, R. J., "Film Cooling," *Advances in Heat Transfer*, Vol. 7, No. C, 1971, pp. 321–379. doi:10.1016/S0065-2717(08)70020-0.
- [16] Hombsch, M., and Olivier, H., "Film cooling in laminar and turbulent supersonic flows," *Journal of Spacecraft and Rockets*, Vol. 50, No. 4, 2013, pp. 742–753. doi:10.2514/1.A32346/ASSET/IMAGES/LARGE/FIGURE27.JPEG.
- [17] Olivier, H., Gronig, H., and Schulze, B., "Instrumentation techniques of the Aachen shock tunnel TH2," Institute of Electrical and Electronics Engineers (IEEE), 2002, pp. 1–116. doi:10.1109/iciiasf.1995.519106.

- [18] Hermann, T., Ifti, H. S., McGilvray, M., Doherty, L., and Geraets, R. P., "Mixing Characteristics in a Hypersonic Flow around a Transpiration Cooled Flat Plate Model," *HiSST: International Conference on High-Speed Vehicle Science Technology*, , No. November, 2018, pp. 1–15.
- [19] Ifti, H. S., Hermann, T., and McGilvray, M., "Transpiration Cooling at Mach 5 Employing Porous UHTC," *Conference on Flight vehicles, Aerothermodynamics and Re-entry Missions and Engineering (FAR)*, 2019, p. 8.
- [20] Ifti, H. S., Hermann, T., Ewenz Rocher, M., Doherty, L., Hambidge, C., McGilvray, M., and Vandeperre, L., "Laminar Transpiration Cooling Experiments in Hypersonic Flow," *Experiments in Fluids*, 2022.
- [21] Ewenz Rocher, M., Hermann, T., McGilvray, M., Ifti, H. S., Vieira, J., Hambidge, C., Quinn, M. K., Grossman, M., and Vandeperre, L., "Pressure-sensitive paint diagnostic to measure species concentration on transpiration-cooled walls," *Experiments in Fluids*, Vol. 63, No. 1, 2022, pp. 1–11. doi:10.1007/S00348-021-03355-9/FIGURES/15.
- [22] Boehrk, H., Wartemann, V., Eggers, T., Martinez Schramm, J., Wagner, A., and Hannemann, K., "Shock Tube Testing of the Transpiration-Cooled Heat Shield Experiment AKTiV," *18th AIAA/3AF International Space Planes and Hypersonic Systems and Technologies Conference*, American Institute of Aeronautics and Astronautics (AIAA), 2012, pp. 1–8. doi:10.2514/6.2012-5935.
- [23] Zaccara, M., Edelman, J. B., and Cardone, G., "A general procedure for infrared thermography heat transfer measurements in hypersonic wind tunnels," *International Journal of Heat and Mass Transfer*, Vol. 163, 2020, p. 120419. doi:10.1016/J.IJHEATMASSTRANSFER.2020.120419, URL <https://www.sciencedirect.com/science/article/pii/S001793102033355X>.
- [24] Falsetti, C., Sisti, M., and Beard, P. F., "Infrared thermography and calibration techniques for gas turbine applications: A review," *Infrared Physics and Technology*, Vol. 113, 2021, p. 103574. doi:10.1016/j.infrared.2020.103574.
- [25] Baehr, H. D., and Stephan, K., *Heat and Mass Transfer*, Springer Berlin Heidelberg, Berlin, Heidelberg, 2011. doi: 10.1007/978-3-642-20021-2.
- [26] Oldfield, M. L., "Impulse response processing of transient heat transfer gauge signals," *Proceedings of the ASME Turbo Expo*, Vol. 3 PART A, American Society of Mechanical Engineers Digital Collection, 2006, pp. 739–750. doi:10.1115/GT2006-90949.
- [27] Hermann, T., McGilvray, M., Ifti, H. S., Hufgard, F., and Löhle, S., "Thermal impulse response in porous media for transpiration-cooling systems," *Journal of Thermophysics and Heat Transfer*, Vol. 34, No. 2, 2020, pp. 447–456. doi:10.2514/1.T5841.
- [28] Schultz, D. L., and Jones, T. V., "Heat-Transfer Measurements In Short-Duration Hypersonic Facilities," *AGARDograph No.165*, 1973.
- [29] McGilvray, M., Doherty, L. J., Neely, A. J., Pearce, R., and Ireland, P., "The Oxford High Density Tunnel," *20th AIAA International Space Planes and Hypersonic Systems and Technologies Conference*, 2015, AIAA American Institute of Aeronautics and Astronautics, 2015.
- [30] Wylie, S., Doherty, L., and McGilvray, M., "Commissioning of the oxford high density tunnel (HDT) for boundary layer stability measurements at mach 7," *2018 Fluid Dynamics Conference*, 2018. doi:10.2514/6.2018-3074.

- [31] Anderson, J. D., “Hypersonic and High-Temperature Gas Dynamics, Third Edition,” *Hypersonic and High-Temperature Gas Dynamics, Third Edition*, 2019. doi:10.2514/4.105142.
- [32] Keyes, F. G., “The Heat Conductivity, Viscosity, Specific Heat and Prandtl Numbers for Thirteen Gases.” Tech. rep., 1952.
- [33] Nield, D., and Bajan, A., *Convection in Porous Media*, 4th ed., Springer, New York, 2013.
- [34] Eckert, E. R. G., “Engineering Relations for Heat Transfer and Friction in High-Velocity Laminar and Turbulent Boundary-Layer Flow Over Surfaces With Constant Pressure and Temperature,” *Journal of Fluids Engineering*, Vol. 78, No. 6, 1956, pp. 1273–1283. doi:10.1115/1.4014011, URL <https://asmedigitalcollection.asme.org/fluidsengineering/article/78/6/1273/1137377/Engineering-Relations-for-Heat-Transfer-and>.
- [35] Schlichting, H., and Gersten, K., “Boundary-Layer Theory,” *Boundary-Layer Theory*, 2016, pp. 1–799. doi:10.1007/978-3-662-52919-5/COVER.
- [36] Ifiti, H. S., “Transpiration Cooling of a Hypersonic Vehicle,” Ph.D. thesis, University of Oxford, 2021.
- [37] Ifiti, H. S., Hermann, T., McGilvray, M., and Merrifield, J., “Numerical Simulation of Transpiration Cooling in a Laminar Hypersonic Boundary-Layer,” *Journal of Spacecraft and Rockets*, 2022.
- [38] Tanno, H., Komuro, T., Itoh, K., Kuhn, M., Petkov, I., and Esser, B., “Transpiration cooling experiments in free-piston shock tunnel HIEST,” *8th European Workshop on Thermal Protection Systems and Hot Structures*, Noordwijk, Nederlande, 2016.
- [39] Gülhan, A., and Braun, S., “An experimental study on the efficiency of transpiration cooling in laminar and turbulent hypersonic flows,” *Experiments in Fluids*, Vol. 50, No. 3, 2011, pp. 509–525. doi:10.1007/s00348-010-0945-6.
- [40] Kays, W. M., “Heat transfer to the transpired turbulent boundary layer,” *International Journal of Heat and Mass Transfer*, Vol. 15, No. 5, 1972, pp. 1023–1044. doi:10.1016/0017-9310(72)90237-2.
- [41] Pappas, C., and Okuno, A. F., “The Relation between Skin Friction and Heat Transfer for the Compressible Turbulent Boundary Layer with Gas Injection,” *NASA TN D-2957*, 1965, p. 32.
- [42] Heufer, K. A., and Olivier, H., “Experimental and Numerical Study of Cooling Gas Injection in Laminar Supersonic Flow,” *AIAA Journal*, Vol. 46, No. 11, 2008, pp. 2741–2751. doi:10.2514/1.34218.
- [43] Meinert, J., J-ogrove, Huhn, r., Serbest, E., and Haidn, O. J., “Turbulent Boundary Layers with Foreign Gas Transpiration,” *Journal of Spacecraft and Rockets*, Vol. 38, No. 2, 2008, pp. 191–198. doi:10.2514/2.3693.
- [44] Coleman, H. W., and Steele, W. G., *Experimentation, Validation, and Uncertainty Analysis for Engineers: Third Edition*, John Wiley and Sons, Hoboken, NJ, USA, 2009. doi:10.1002/9780470485682.
- [45] Astarita, T., and Carlomagno, G. M., *Infrared Thermography for Thermo-Fluid-Dynamics*, Springer Berlin Heidelberg, 2013. doi:10.1007/978-3-642-29508-9.

VII. Uncertainty Analysis

The main independent quantities measured in this paper are the Stanton number, the blowing ratio, the blowing parameter and the freestream unit Reynolds number. To find the total uncertainty, the Taylor Series Method by Coleman and Steele [44] was employed where, for a function $r = r(X_1, X_2, \dots, X_n)$, the uncertainties in the individual measurements are assumed to be uncorrelated. Thereafter, gradients $\frac{\partial r}{\partial X_i}$ are calculated numerically by perturbing the variables X_i in the data reduction processing steps. First of all, the unit Reynolds number is calculated according to the following equation

$$Re_u = \frac{\rho_e u_e}{\mu_e} \quad (17)$$

where u_e and ρ_e are a function of the Mach number, M , total pressure, P_0 , and total temperature, T_0 . The Stanton number, is calculated according to

$$St = \frac{\dot{q}_w}{\rho_e u_e c_p (T_0 - T_w)} \quad (18)$$

where the heat flux at the wall, \dot{q}_w , is a function of the material thermal effusivity, $\sqrt{\rho c_p k}$, and the temperature, T_w , obtained through infrared camera measurements. The blowing ratio is calculated using Eq. 4, which depends on T_e and ρ_e as well as the injected mass flux, $\rho_f u_f$. This is calculated assuming a linear pressure gradient through the porous injector and a constant solid temperature by employing Eq (10). The uncertainties in the Darcy and Forchheimer coefficients were determined using the same monte carlo simulation procedure detailed in Ref [7]. The blowing parameter relates the uncooled Stanton number and the blowing ratio as per Eq (3). The free-stream mass flux cancels out in this equation and can be written as

$$B_h = \frac{\rho_f u_f c_p (T_0 - T_w)}{\dot{q}_w} \quad (19)$$

where, in this case, there is no dependency on Mach number, M , or total pressure, P_0 .

The wall temperature, T_w is determined via infrared thermography and a key figure of merit used to qualify the temperature output of infrared cameras is the noise equivalent differential temperature (NETD) [45]. This is a signal-to-noise figure that represents the temperature difference which would produce a signal equal to the camera's temporal noise. For both the FLIR A6751 SLS and Telops M3K cameras used in this work, a factory calibration determined that the NETD was below 40 mK over the observed range of temperatures. This is significantly smaller than the expected temperature rise of the injector of 0.5-5 K. In addition to the NETD, there are additional sources of error from the infrared calibration system. This includes the error in the measurement of the reflected temperature when conducting the multipoint calibration, T_{ref} , and the error in the temperature measurement of the CI-Systems black body

calibrator, $T_{\text{calibrator}}$. Finally, to go from the black body temperature to the temperature of the material of interest, the emissivity of the material, ε , is required.

Table 4 lists the different uncertainty contributions to the overall uncertainty in the measurement of Reynolds number, Stanton number, blowing ratio and blowing parameter for the case of a injected mass flux of $0.833 \text{ kg s}^{-1} \text{ m}^{-2}$. This represents a medium level of Nitrogen injection for the METAPOR CE170 injector. The main drivers of uncertainty, especially for the Stanton number and blowing parameter are the total temperature, T_0 , and the material thermal effusivity. The uncertainty in blowing parameter is 14.0% where the main source of uncertainty is the uncertainty in the total temperature (60%). A tighter measurement of total temperature in future experimental campaigns and higher accuracy materials may yield uncertainties well below 10% for all of the key independent quantities.

Table 4 Uncertainty contributions and overall uncertainties in unit Reynolds number, uncooled Stanton number, blowing ratio, and blowing parameter. This is for the laminar freestream condition with Nitrogen injection at $0.833 \text{ kg s}^{-1} \text{ m}^{-2}$ and a METAPOR CE170 injector.

Parameter	Baseline value	Absolute uncertainty	Relative uncertainty
NETD (K)	0.04	± 0.02	50%
T_{ref} (K)	296	± 2	<1%
$T_{\text{calibrator}}$ (K)	296	± 0.1	<1%
ε	0.95	± 0.04	4.2%
$(\sqrt{\rho c k}) (\text{Jm}^{-2} \text{K}^{-1} \text{s}^{-0.5})$	1565	± 78.25	5%
P_0 (kPa)	1204	± 24.08	2%
T_0 (K)	420	± 10	2.4%
M	6.1	± 0.1	1.6%
T_{pl} (K)	293	± 2	<1%
p_{pl} (K)	$3.89 \cdot 10^5$	$\pm 1 \cdot 10^4$	2.5%
K_D	$2.52 \cdot 10^{-13}$	$\pm 1.74 \cdot 10^{-14}$	6.9%
K_F	$1.03 \cdot 10^{-8}$	$\pm 1.06 \cdot 10^{-9}$	10.3%
Re_u	$13.3 \cdot 10^6$	$\pm 6.26 \cdot 10^5$	4.7%
St_0	$5 \cdot 10^{-3}$	$\pm 6.45 \cdot 10^{-4}$	12.9%
F	$1.7 \cdot 10^{-2}$	$\pm 1.2 \cdot 10^{-3}$	7.1%
B_h	3.43	± 0.48	14.0%